Limiting amplitude principle and resonances in plasmonic structures with corners: Numerical investigation

Camille Carvalho[a,*], Patrick Ciarlet Jr.[b], Claire Scheid[c]

[a] *Applied Math Department, University of California Merced, 5200 N Lake Rd, Merced, CA 95348, United States*
[b] *POEMS, CNRS, INRIA, ENSTA Paris, Institut Polytechnique de Paris, 91120 Palaiseau, France*
[c] *Université Côte d'Azur, CNRS, INRIA, LJAD, 06103 Nice, France*

Abstract

The limiting amplitude principle states that the response of a scatterer to a harmonic light excitation is asymptotically harmonic with the same pulsation. Depending on the geometry and nature of the scatterer, there might or might not be an established theoretical proof validating this principle. In this paper, we investigate a case where the theory is missing: we consider a two-dimensional dispersive Drude structure with corners. In the non lossy case, it is well known that looking for harmonic solutions leads to an ill-posed problem for a specific range of critical pulsations, characterized by the metal's properties and the aperture of the corners. Ill-posedness is then due to highly oscillatory resonances at the corners called black-hole waves. However, a time-domain formulation with a harmonic excitation is always mathematically valid. Based on this observation, we conjecture that the limiting amplitude principle might not hold for all pulsations. Using a time-domain setting, we propose a systematic numerical approach that allows to give numerical evidences of the latter conjecture, and find clear signature of the critical pulsations. Furthermore, we connect our results to the underlying physical plasmonic resonances that occur in the lossy physical metallic case.

1. Introduction

Plasmonic structures are commonly made of noble metals (silver, gold, etc.) and dielectrics (air, vacuum, glass). At optical frequencies, metals can be dispersive, allowing the propagation of localized surface waves at the metal–dielectric interface called surface plasmons [1]. The field of plasmonics is very active as surface plasmons offer strong light enhancement, with applications to next-generation sensors, antennas, high-resolution imaging, cloaking and other [2–7]. Several models are available in the literature to model dispersive materials. In particular, Drude model [8] is relevant for classical noble materials: in this approximation, the metal is considered as a free electrons gas (with a static lattice of positive ions). Then interactions of these electrons with the ion lattice manifest through a collision frequency parameter, representing dissipation in the equations. Over the past decades, new models

---

* Corresponding author.
  E-mail address: ccarvalho3@ucmerced.edu (C. Carvalho).

have been developed, including the so-called negative-index metamaterial, and interesting ideal cases (negligible dissipation) have been uncovered.

If the source of incident illumination is monochromatic, one would naturally expect the time dependent electromagnetic field to evolve asymptotically (in time) to a harmonic state with the corresponding incident frequency. This asymptotic harmonic behavior is called *Limiting amplitude principle* and allows to work with the associated frequency-domain boundary value problem. The limiting amplitude principle has been investigated for a long time, and is well understood for the wave equation and related classical scattering problems [9–13]. Recently there has been a new interest in exploring this principle in the context of emerging plasmonic structures [14,15]. In particular, the specific case of a planar interface with a non lossy Lorentz model has been fully investigated in [15]. However for other configurations, the landscape is different: this is especially not clear for (non lossy) plasmonic structures with corners.

The limiting amplitude principle is closely related to well-posedness of the corresponding harmonic equation. Although the time-dependent equations system is mathematically well-posed (in the usual function spaces), the frequency-domain counterpart has proven to be more challenging [16–22]. A key point lies in the fact that the Fourier transform of a non lossy metal's constitutive law can correspond to a real negative permittivity.[1] The induced possible change of sign of the permittivity at the interface affects the optical response. If the structure has corners, the frequency-domain equations system may be mathematically ill-posed for a range of critical frequencies (corresponding to a critical range of permittivities). In this range of frequencies, hypersingular behaviors arise at the interface (especially at corners), requiring specific numerical treatments to avoid spurious reflections and inaccurate predictions. Ill-posedness in frequency-domain corresponds to an unphysical *infinite* electromagnetic energy, indicating that *the limiting amplitude principle should not hold in that case*. This conjecture motivates our exploration.

In this paper we provide a systematic approach to numerically assess the latter conjecture in non lossy subwavelength plasmonic structures with corners. We base our strategy on a time-domain framework. From typical quantities of interest (fields, energy, cross sections, Poynting flux, etc.), we manage to identify a signature of the underlying critical interval from the frequency-domain, by using time-domain simulations. Our results show a clear change of behavior at critical frequencies. Additionally, we find this signature also when considering physical structures (incorporating losses): in other words the limit non lossy case is useful to highlight intrinsic resonances in physical plasmonic structures.

The paper is organized as follows. Section 2 presents the general context, the model problem along with relevant quantities of interest. In Section 3, we specify the two-dimensional (or 2D), geometrical, physical and numerical framework that we precisely consider to explore the limiting amplitude principle. The numerical evidences that assess our conjecture are detailed in Section 4. Then, in Section 5, we continue our efforts towards a more physical discussion. Finally Section 6 presents our concluding remarks.

2. General context: plasmonics and limiting amplitude principle

2.1. Drude model in plasmonics

As mentioned in the introduction, plasmonic structures are commonly made of noble metals and dielectrics, where surface plasmons arise at the interface at optical frequencies. We present below the well-known Drude model and related equations to model the electromagnetic field in those structures.

Metals at optical frequencies are known to be dispersive: each monochromatic wave travels with different speeds through the metallic material. To accurately model optical properties of metallic structures, one has thus to rely on models that take into account the frequency-dependent velocity of the wave. This dispersion phenomenon is equivalently explained as a delay effect in the reaction of the electrons of the metal to light excitation. In this work, we will use the well-known Drude model to account for this dispersion phenomenon. It is based on the kinetic theory of gases [8], considering the metal as a static lattice of positive ions immersed in a free electrons gas. In the case of scattering by a metallic obstacle, the set of (linearized) equations can be eventually summarized as follows.

The time-dependent electromagnetic field is computed using time-domain Maxwell's equations with variables $(\mathbf{D}, \mathbf{E}, \mathbf{B}, \mathbf{H})$[2] where dispersive effects are incorporated through the electric constitutive law. The latter relates the

---

[1] It commonly provides some imaginary part for lossy materials.

[2] Respectively electric displacement, electric field, magnetic induction, magnetic field.

electric displacement **D** and the electric field **E** and incorporates the possible time history (when dispersive effects are taken into account) via a time convolution (denoted $*_t$):

$$\mathbf{D} = \varepsilon *_t \mathbf{E}, \tag{1}$$

where

$$\varepsilon(t, \cdot) := \delta_0(t)\varepsilon_0\varepsilon_r(\cdot) + \chi(t, \cdot), \tag{2}$$

is the space–time dielectric permittivity, ε_0 the vacuum permittivity, ε_r the relative permittivity and χ is the electric sensitivity. These quantities are defined in $\mathbb{R}^3$ and such that causality property holds (see *e.g.* [23] for a nice review). Since we do not take any dispersive effects into account in the dielectric, one sets $\chi = 0$ there. However, in the metallic obstacle, χ is non vanishing. If one defines the polarization current **J** as $\mathbf{J} := -\partial_t(\chi *_t \mathbf{E})$, one can rewrite the whole set of Maxwell's equations in terms of $(\mathbf{E}, \mathbf{H}, \mathbf{J})$ variables only. In particular, **J** verifies a linear differential equation that is linearly coupled to $(\mathbf{E}, \mathbf{H})$ through classical Maxwell's equations. With this approach, we do not need the expression of χ explicitly. The reason is that Drude model is entirely determined via the variable **J** (see below). We will see later that χ plays an important role in frequency-domain.

We fix an *end time* $T > 0$, and a *domain* Ω, that is an open and connected subset of $\mathbb{R}^3$ with Lipschitz boundary. In our model, the domain Ω is the metallic obstacle, and it is immersed in a homogeneous dielectric background. For the practical choice of the end time T in numerical simulations, we refer to Section 3.4. In what follows, μ_0 denotes the permeability of vacuum, ε_d denotes the dielectric relative permittivity of the dielectric and ε_∞ the relative permittivity (at infinite frequency) of the metallic obstacle Ω. We now set

$$\varepsilon_r(\mathbf{x}) := \begin{cases} \varepsilon_d, & \text{for } \mathbf{x} \in \mathbb{R}^3 \setminus \bar{\Omega}, \\ \varepsilon_\infty, & \text{for } \mathbf{x} \in \Omega, \end{cases} \tag{3}$$

and we will denote $\varepsilon := \varepsilon_0\varepsilon_r$. Thereafter, Drude model in the time-domain writes on $[0, T]$ as:

$$\mu_0 \frac{\partial \mathbf{H}}{\partial t} = -\mathbf{curl}\, \mathbf{E} \ \text{ in } \mathbb{R}^3, \tag{4a}$$

$$\varepsilon_0\varepsilon_d \frac{\partial \mathbf{E}}{\partial t} = \mathbf{curl}\, \mathbf{H} + \mathbf{J}_{ext} \ \text{ in } \mathbb{R}^3 \setminus \bar{\Omega}, \tag{4b}$$

$$\varepsilon_0\varepsilon_\infty \frac{\partial \mathbf{E}}{\partial t} = \mathbf{curl}\, \mathbf{H} - \mathbf{J} + \mathbf{J}_{ext} \ \text{ in } \Omega, \tag{4c}$$

$$\frac{\partial \mathbf{J}}{\partial t} = \omega_p^2\varepsilon_0\mathbf{E} - \gamma\mathbf{J} \ \text{ in } \Omega, \tag{4d}$$

$$\mathbf{J} = 0, \ \text{ in } \mathbb{R}^3 \setminus \bar{\Omega}, \tag{4e}$$

where ω_p is the plasma angular frequency, and γ the collision frequency (coming from Drude model). Here $\mathbf{J}_{ext}$ denotes a possible external current that we will use to model volumic source excitation in the following.

Remark 1.   Note that the plasma angular frequency characterizes the angular frequency above which an incident wave can completely penetrate the metal. On the other hand, the strong plasmonic effects induced by surface plasmons are obtained by an illumination, below the plasma angular frequency, of subwavelength metallic structures.

We will call this system *time-dependent Maxwell–Drude equations in plasmonic structures*.

Well-posedness. As commonly done, in order to compute the solution, we will artificially truncate the *exterior domain* $\mathbb{R}^3 \setminus \bar{\Omega}$ and close the system (4) by adding approximate transparent boundary conditions (for **E** and **H**), transmission conditions at $\partial\Omega$ (for **E** and **H**) and initial conditions (for **E**, **H** and **J**). At the artificial boundary, to approximate transparent boundary conditions, we will use classical first order Silver–Müller boundary conditions. In this setting, using classical semi-group theory, one can prove that system (4) is well posed[3] (see e.g. [24] for details).

---

[3] This result is obtained in the natural space $\mathcal{C}^0([0, T], H(\mathbf{curl})) \times \mathcal{C}^0([0, T], H(\mathbf{curl})) \times \mathcal{C}^0([0, T], L^2)$ with L^2 tangential traces for **E** and **H**.

Excitation. Several excitations of the scatterer are possible. A physically compliant one consists of using an incident illumination that we denote $(\mathbf{E}_{inc}, \mathbf{H}_{inc})$. To take this illumination into account in the set of equations, we use the non homogeneous Silver–Müller boundary conditions as:

$$\mathbf{n} \times \mathbf{E} - \mathbf{n} \times (\sqrt{\frac{\mu_0}{\varepsilon_0}} \mathbf{H} \times \mathbf{n}) = \mathbf{n} \times \mathbf{g_{inc}}, \tag{5}$$

with $\mathbf{g_{inc}} = \mathbf{E}_{inc} - (\sqrt{\frac{\mu_0}{\varepsilon_0}} \mathbf{H}_{inc} \times \mathbf{n})$ and $\mathbf{n}$ the outward normal to the exterior artificial boundary.

Remark 2. As a result, the total electromagnetic field $(\mathbf{E}, \mathbf{H})$ can be decomposed into an incident contribution $(\mathbf{E}_{inc}, \mathbf{H}_{inc})$ and a scattered one $(\mathbf{E}_{sca}, \mathbf{H}_{sca})$. The scattered field $(\mathbf{E}_{sca}, \mathbf{H}_{sca})$ verifies Maxwell's equations with homogeneous radiation condition and a source term $\mathbf{J}_{ext}$.

Electromagnetic energy, Poynting vector. We define the time-dependent total energy of system (4) by

$$\mathcal{E}(t) = \frac{1}{2} \| \sqrt{\varepsilon_0 \varepsilon_r} \mathbf{E}(., t) \|^2_{L^2(\mathbb{R}^3)} + \frac{1}{2} \| \sqrt{\mu_0} \mathbf{H}(., t) \|^2_{L^2(\mathbb{R}^3)} + \frac{1}{2\varepsilon_0 \omega_p^2} \| \mathbf{J}(., t) \|^2_{L^2(\mathbb{R}^3)}. \tag{6}$$

The space–time dependent Poynting vector also plays a central role in the study of the energy's variations, classically defined as

$$\Pi = \mathbf{E} \times \mathbf{H}. \tag{7}$$

Recalling that we have $\operatorname{div}(\mathbf{E} \times \mathbf{H}) = \mathbf{H} \cdot \mathbf{curl}\, \mathbf{E} - \mathbf{E} \cdot \mathbf{curl}\, \mathbf{H}$, formally we get, using Eqs. (4)

$$\begin{aligned}
\frac{\partial \mathcal{E}}{\partial t}(t) &= \int_{\mathbb{R}^3} (\operatorname{div}(\mathbf{E}(\mathbf{x}, t) \times \mathbf{H}(\mathbf{x}, t)) + \mathbf{J}_{ext}(\mathbf{x}, t) \cdot \mathbf{E}(\mathbf{x}, t)) d\mathbf{x} \\
&\quad + \int_{\Omega} \mathbf{J}(\mathbf{x}, t) \cdot \mathbf{E}(\mathbf{x}, t) - \mathbf{E}(\mathbf{x}, t) \cdot \mathbf{J}(\mathbf{x}, t) d\mathbf{x} - \frac{\gamma}{\varepsilon_0 \omega_p^2} \int_{\Omega} \mathbf{J}(\mathbf{x}, t) \cdot \mathbf{J}(\mathbf{x}, t) d\mathbf{x}, \\
&= \int_{\mathbb{R}^3} \operatorname{div}(\Pi(\mathbf{x}, t)) d\mathbf{x} + \int_{\mathbb{R}^3} \mathbf{J}_{ext}(\mathbf{x}, t) \cdot \mathbf{E}(\mathbf{x}, t) d\mathbf{x} - \frac{\gamma}{\varepsilon_0 \omega_p^2} \int_{\Omega} \mathbf{J}(\mathbf{x}, t) \cdot \mathbf{J}(\mathbf{x}, t) d\mathbf{x}.
\end{aligned} \tag{8}$$

The pointwise version of the equality is the Poynting theorem. From (8), we deduce that if $\mathbf{J}_{ext} \equiv 0$, $\operatorname{div}(\Pi(\mathbf{x}, t)) \equiv 0$ and $\gamma = 0$, then the energy is preserved. If $\mathbf{J}_{ext} \equiv 0$ and the quantity $\operatorname{div}(\Pi(\mathbf{x}, t)) \leq 0$, then the energy is dissipated. In the rest of the paper, we focus on the limit case where there is no physical dissipation, i.e. $\gamma = 0$.

Remark 3. When using first order Silver–Müller boundary conditions, we introduce artificial dissipation in the system and as a result $\operatorname{div}(\Pi(\mathbf{x}, t)) \leq 0$ if the condition is homogeneous.

Long time asymptotics. If the source is monochromatic, one would naturally expect the solution to evolve asymptotically (in time) to a harmonic state with the corresponding incident frequency. This asymptotic harmonic behavior is called *Limiting amplitude principle*. This principle holds for standard settings and is closely related to well-posedness of the corresponding harmonic equation. This principle is well-understood in classic dielectric materials. However in the non lossy case and for objects with corners, the landscape is different and less trodden.

2.2. Limiting amplitude principle

The limiting amplitude principle has been studied for a long time (e.g. [9–13]) and states the following. Given a source $t \mapsto e^{-i\omega t} \mathbf{F}(.)$, with $\mathbf{F} \in L^2(\mathbb{R}^3)$ (and support $\operatorname{supp}\mathbf{F} \Subset \mathbb{R}^3$), a given pulsation $\omega > 0$, and a problem of the form $\partial_t^2 \mathbf{U} + \mathcal{L}\mathbf{U} = e^{-i\omega t}\mathbf{F}$, with $\mathcal{L}$ a linear differential operator, then after a long time the solution asymptotically behaves as $\mathbf{U} = e^{-i\omega t}\mathbf{W}$ with $\mathbf{W}$ satisfying a problem of the form $-\omega^2\mathbf{W} + \mathcal{L}\mathbf{W} = \mathbf{F}$.

This statement indicates that a periodic regime is asymptotically established and therefore it is natural to consider the problem in the time-harmonic regime (stationary problem).

Assume for now we can write the external current $\mathbf{J}_{ext}(\mathbf{x}, t) = \Re(\underline{\mathbf{J}}_{ext}(\mathbf{x})e^{-i\omega t})$, and $(\mathbf{E}, \mathbf{H}, \mathbf{J})(\mathbf{x}, t) = \Re(\underline{\mathbf{E}}(\mathbf{x})e^{-i\omega t}, \underline{\mathbf{H}}(\mathbf{x})e^{-i\omega t}, \underline{\mathbf{J}}(\mathbf{x})e^{-i\omega t})$, with $\underline{\mathbf{J}}_{ext}, \underline{\mathbf{E}}, \underline{\mathbf{H}}, \underline{\mathbf{J}}$ denoting complex-valued fields. Then system (4) (with $\gamma = 0$)

simplifies to

$$-i\omega\mu_0\underline{\mathbf{H}} = -\mathbf{curl}\,\underline{\mathbf{E}} \quad \text{in } \mathbb{R}^3, \tag{9a}$$

$$-i\omega\varepsilon_0\hat{\varepsilon}_r\underline{\mathbf{E}} = \mathbf{curl}\,\underline{\mathbf{H}} + \underline{\mathbf{J}}_{ext} \quad \text{in } \mathbb{R}^3, \tag{9b}$$

with

$$\hat{\varepsilon}_r(\mathbf{x}, \omega) := \begin{cases} \varepsilon_d > 0, & \text{for } \mathbf{x} \in \mathbb{R}^3 \setminus \bar{\Omega}, \\ \varepsilon_m(\omega) = \left(\varepsilon_\infty - \frac{\omega_p^2}{\omega^2}\right), & \text{for } \mathbf{x} \in \Omega, \end{cases} \tag{10}$$

and transmission conditions, plus some radiation condition at infinity. Indeed, $\underline{\mathbf{J}}$ is known, and equal to $i\frac{\omega_p^2\varepsilon_0}{\omega}\underline{\mathbf{E}}$ in Ω, respectively 0 in $\mathbb{R}^3 \setminus \bar{\Omega}$. We will also denote $\hat{\varepsilon} := \varepsilon_0\hat{\varepsilon}_r$. Above $\varepsilon_0\varepsilon_m(\omega)$ represents the non lossy Drude model permittivity. Let us point out that if $0 < \omega < \frac{\omega_p}{\sqrt{\varepsilon_\infty}}$ (optical frequency range), then $\varepsilon_m(\omega) < 0$. System (9) will be called the *frequency-dependent Maxwell–Drude equations in plasmonic structures*.

Remark 4. We make the abuse of terminology to denote ω by the terms pulsation, frequency, or angular frequency. However in numerical experiments, ω will be always given in rad s^{-1}.

Well-posedness. Classical theory considers $\underline{\mathbf{E}}, \underline{\mathbf{H}} \in \mathbf{H}_{loc}(\mathbf{curl}) := \{\mathbf{X} \in L^2_{loc}(\mathbb{R}^3) | \forall \xi \in \mathcal{C}^\infty_c(\mathbb{R}^3), \xi\mathbf{X} \in \mathbf{H}(\mathbf{curl})\}$, and (9) is equivalent to solve:

$$\mathbf{curl}\,\hat{\varepsilon}_r^{-1}\mathbf{curl}\,\underline{\mathbf{H}} - k^2\underline{\mathbf{H}} = -\mathbf{curl}\,\hat{\varepsilon}_r^{-1}\underline{\mathbf{J}}_{ext} \quad \text{in } \mathbb{R}^3, \tag{11a}$$

$$-i\omega\varepsilon_0\hat{\varepsilon}_r\underline{\mathbf{E}} = \mathbf{curl}\,\underline{\mathbf{H}} + \underline{\mathbf{J}}_{ext} \quad \text{in } \mathbb{R}^3, \tag{11b}$$

with $k = \omega\sqrt{\varepsilon_0\mu_0}$. One can also consider the system

$$-i\omega\mu_0\underline{\mathbf{H}} = -\mathbf{curl}\,\underline{\mathbf{E}} \quad \text{in } \mathbb{R}^3, \tag{12a}$$

$$\mathbf{curl}\,\mathbf{curl}\,\underline{\mathbf{E}} - k^2\hat{\varepsilon}_r\underline{\mathbf{E}} = -i\omega\mu_0\mathbf{curl}\,\underline{\mathbf{J}}_{ext} \quad \text{in } \mathbb{R}^3. \tag{12b}$$

Note that, if one chooses $\underline{\mathbf{J}}_{ext}$ so that $\text{div}(\underline{\mathbf{J}}_{ext}) = 0$, then $(\underline{\mathbf{E}}, \underline{\mathbf{H}}) \in \mathbf{H}_{loc}(\mathbf{curl})^2$ solution of (12) or (11) also belongs to $\mathbf{V}_{loc}(\hat{\varepsilon}; \mathbf{curl}) \times \mathbf{V}_{loc}(\mu_0; \mathbf{curl})$, with $\mathbf{V}_{loc}(\zeta; \mathbf{curl}) := \{\mathbf{X} \in \mathbf{H}_{loc}(\mathbf{curl}) | \text{div}(\zeta\mathbf{X}) = 0\}$.

Contrary to the time-domain case, due to the change of sign of $\hat{\varepsilon}_r$ at optical frequencies, the problems (11)–(12) can be ill-posed in $\mathbf{V}_{loc}(\hat{\varepsilon}; \mathbf{curl}) \times \mathbf{V}_{loc}(\mu_0; \mathbf{curl})$. With the T-coercivity approach it has been shown (e.g. [16–18,20,21,25,26]) that there exists two cases depending on *the contrast* $\kappa_\varepsilon := \frac{\varepsilon_m}{\varepsilon_d}$:

- for contrasts κ_ε *far enough* from -1, then the problem is well-posed in $\mathbf{V}_{loc}(\hat{\varepsilon}; \mathbf{curl}) \times \mathbf{V}_{loc}(\mu_0; \mathbf{curl})$.
- for contrasts κ_ε *close to* -1, plasmonic hypersingularities arise at the corners of the interface (if any), and the problems is ill-posed in $\mathbf{V}_{loc}(\hat{\varepsilon}; \mathbf{curl}) \times \mathbf{V}_{loc}(\mu_0; \mathbf{curl})$.

Those guidelines can be refined for the specific case of Maxwell 2D. In that case the interval of contrasts (acceptable or not) is explicitly known. For now, let us denote I_c this interval. We will provide explicit bounds if needed for numerical purposes. Let us note that this interval I_c corresponds to a *critical interval* of angular frequencies I_ω, and that it holds that

$$\kappa_\varepsilon = -1 \quad \text{if, and only if,} \quad \omega := \omega_{sp} := \frac{\omega_p}{\sqrt{\varepsilon_d + \varepsilon_\infty}} \tag{13}$$

with ω_{sp} denoting the surface plasmon angular frequency. The specific case $\omega = \omega_{sp}$ is very peculiar and the problem is strongly-ill posed. In what follows we will exclude this case.

To sum up, in the frequency-domain, there is a critical range of angular frequencies for which the problem is then ill-posed, whereas in the time-domain the problem is always mathematically well-posed. This interesting result questions the validity of the limiting amplitude principle at critical angular frequencies, indicating that

- If $\omega \notin I_\omega$: the limiting amplitude principle holds.
- If $\omega \in I_\omega$: the limiting amplitude should not hold.

Using this conjecture, the rest of the paper is dedicated to provide several approaches and results to find signature of the critical interval I_ω in time-domain simulations. To that aim we will need to compute quantities of interest in frequency-domain.

Remark 5. The limiting amplitude principle has been studied for Lorentz metamaterials (both permeability and permittivity can change sign in frequency-domain) for planar interfaces. It has been shown that this principle does not hold for $\kappa_\varepsilon = -1$, and that in this case the fields' amplitude increases linearly with respect to time [15].

Electromagnetic energy, Poynting vector and cross sections. Time-domain quantities such as the electromagnetic energy and the Poynting vector can be compared to frequency-domain ones if harmonic behavior is achieved. In the time-domain, we consider a real-valued harmonic excitation of the form $\mathbf{J}_{ext}(\mathbf{x}, t) = \Re(\underline{\mathbf{J}}_{ext}(\mathbf{x})e^{-i\omega t})$, with $\omega > 0$ and $\underline{\mathbf{J}}_{ext}$ a complex-valued field. If we denote $(\underline{\mathbf{E}}, \underline{\mathbf{H}})$ the solution of (9) with source term $\underline{\mathbf{J}}_{ext}$, then if the solution of (4) is harmonic, it should write as $(\mathbf{E}(\mathbf{x}, t), \mathbf{H}(\mathbf{x}, t), \mathbf{J}(\mathbf{x}, t)) = \Re(\underline{\mathbf{E}}(\mathbf{x})e^{-i\omega t}, \underline{\mathbf{H}}(\mathbf{x})e^{-i\omega t}, \underline{\mathbf{J}}(\mathbf{x})e^{-i\omega t})$. Then to relate frequency- and time-domain energy, the adequate quantity to start with is the time average energy

$$\underline{\mathcal{E}} = \frac{1}{T(\omega)} \int_{t_0}^{t_0+T(\omega)} \mathcal{E}(t)dt, \tag{14}$$

where $T(\omega)$ is equal to the time period, i.e. $T(\omega) = 2\pi\omega^{-1}$, and $t_0 \geq 0$. Using expression (6), the average energy becomes[4]

$$\begin{aligned}
\underline{\mathcal{E}} &= \frac{1}{2T(\omega)} \int_{t_0}^{t_0+T(\omega)} \|\frac{\sqrt{\varepsilon}}{2}(\underline{\mathbf{E}}e^{-i\omega t} + \underline{\mathbf{E}}^* e^{i\omega t})\|_{L^2(\mathbb{R}^3)}^2 + \|\frac{\sqrt{\mu_0}}{2}(\underline{\mathbf{H}}e^{-i\omega t} + \underline{\mathbf{H}}^* e^{i\omega t})\|_{L^2(\mathbb{R}^3)}^2 \\
&\quad + \frac{1}{\varepsilon_0\omega_p^2}\|\frac{1}{2}(\underline{\mathbf{J}}e^{-i\omega t} + \underline{\mathbf{J}}^* e^{i\omega t})\|_{L^2(\mathbb{R}^3)}^2 dt, \\
&= \frac{1}{4}\left(\|\sqrt{\varepsilon}\underline{\mathbf{E}}\|_{L^2(\mathbb{R}^3)}^2 + \|\sqrt{\mu_0}\underline{\mathbf{H}}\|_{L^2(\mathbb{R}^3)}^2 + \frac{1}{\varepsilon_0\omega_p^2}\|\underline{\mathbf{J}}\|_{L^2(\mathbb{R}^3)}^2\right),
\end{aligned} \tag{15}$$

with $\underline{\mathbf{V}}^*$ denoting the complex conjugate of $\underline{\mathbf{V}}$.

Remark 6. We here point out a very straightforward fact that will be used later in the computations. For the time-domain fields to have a harmonic behavior, the time average of the energy on an interval of length $T(\omega)$ must not depend on the chosen interval. This simple remark provides us with a necessary condition for a signal to be harmonic.

Similarly, we can compute the time average Poynting vector over the time period $T(\omega)$ defined as follows:

$$\underline{\Pi}(\omega) = \frac{1}{T(\omega)} \int_{t_0}^{t_0+T(\omega)} \Pi(t)dt = \frac{1}{2}\Re(\underline{\mathbf{E}} \times \underline{\mathbf{H}}^*). \tag{16}$$

We will omit to write the space dependence using the abuse of notations $\underline{\Pi}(\omega) = \underline{\Pi}(\cdot, \omega)$, $\Pi(t) = \Pi(\cdot, t)$.

To further exploit information from the Poynting vector, it is natural to introduce physical quantities called cross sections. As introduced in Remark 2, we separate the contributions from the scattered fields $(\mathbf{E}_{sca}, \mathbf{H}_{sca})$ and the incident fields $(\mathbf{E}_{inc}, \mathbf{H}_{inc})$: we define $\Pi_{sca} = \mathbf{E}_{sca} \times \mathbf{H}_{sca}$, $\underline{\Pi}_{sca}(\omega) = \frac{1}{T(\omega)} \int_{t_0}^{t_0+T(\omega)} \Pi_{sca}(t)dt$, and similarly $\underline{\Pi}_{inc}$ using the incident electromagnetic fields. Note that $|\underline{\Pi}_{inc}|$ is independent of the spatial variables.

To quantify the amount of absorbed energy $\underline{P}_{abs}$ and scattered energy $\underline{P}_{sca}$ at a given pulsation, we compute the fluxes of, respectively, the total Poynting vector $\underline{\Pi}$ and the scattered Poynting vector $\underline{\Pi}_{sca}$ on a closed surface S enclosing the scatterer:

$$\underline{P}_{abs}(\omega) =: -\int_S \underline{\Pi}(\omega) \cdot \mathbf{n}dS, \quad \underline{P}_{sca}(\omega) =: -\int_S \underline{\Pi}_{sca}(\omega) \cdot \mathbf{n}dS, \tag{17}$$

where $\mathbf{n}$ is the outward normal vector to S. If one denotes by V the bounded volume such that $S = \partial V$, one has obviously $\underline{P}_{abs}(\omega) = -\int_V \text{div}\underline{\Pi}(\omega)d\mathbf{x}$. If there is a scatterer in the domain, not all the energy entering the volume delimited by S will leave it: some energy is absorbed ($\underline{P}_{abs}(\omega) > 0$). The cross sections are then defined relative to the power density (per unit area) of the incident field:

$$C_{abs} = \frac{\underline{P}_{abs}}{|\underline{\Pi}_{inc}|}, \quad C_{sca} = \frac{\underline{P}_{sca}}{|\underline{\Pi}_{inc}|}, \tag{18}$$

---

[4] Recall that $\underline{\mathbf{J}} = 0$ in $\mathbb{R}^3 \setminus \bar{\Omega}$.

where C_{abs} denotes the absorption cross section, C_{sca} the scattering cross section.[5] These frequency-domain quantities are widely used to measure the absorption or the scattering features of a given scatterer. For some standard structures, it is also possible to have their analytical expression (see *e.g.* [27] and references therein).

3. The two-dimensional case: theoretical and numerical guidelines

We focus on the light scattering by a rod structure with transversal section $\mathbb{D}$. We seek solutions of system (4) that have an invariance with respect to the direction of the rod's axis. In this setting the tridimensional Maxwell's equations can be recast in two 2D sets of equations defining two transverse modes: TE (Transverse Electric) and TM (Transverse Magnetic).

In the rest of this paper, we consider that Ω is a metallic rod of bounded section $\mathbb{D}$, $\Omega := \mathbb{D} \times \mathbb{R}$ and we concentrate on the 2D TM polarization. Then $(\vec{E}_\perp, H_z, \vec{J}_\perp)$, with $\vec{V}_\perp := (V_x, V_y)^t$, is solution of the corresponding two-dimensional version of Maxwell's equations.

3.1. An explicit theoretical critical interval

As mentioned previously, there exists a critical interval I_ω, centered around the surface plasmon frequency ω_{sp}, for which the problem is ill-posed in frequency-domain. In some cases, this interval is explicitly known, and hypersingular behaviors have been identified in the ill-posed configurations. We will use this framework to assert if the limiting amplitude principle holds.

According to (11a), in frequency-domain, the problem in $\underline{H}_z$ becomes

$$\operatorname{curl} \hat{\varepsilon}_r^{-1} \mathbf{curl}\, \underline{H}_z - k^2 \underline{H}_z = -\operatorname{curl} \hat{\varepsilon}_r^{-1} \vec{J}_{ext,\perp} \text{ in } \mathbb{R}^2,$$

and similarly for the problem in $\underline{\vec{E}}_\perp$ (cf. (12b)). Classical theory considers $\underline{\vec{E}}_\perp \in \mathbf{L}^2_{loc}(\mathbb{R}^2)$ so that $\underline{H}_z \in H^1_{loc}(\mathbb{R}^2)$, and the bounds of the interval I_c depends on the interface's geometry. Suppose that the interface $\Sigma := \partial \mathbb{D}$ is polygonal with $0 < \alpha < 2\pi$ the sharpest interior angle in $\mathbb{D}$. We define $I_\alpha := \max\left(\frac{\alpha}{2\pi - \alpha}; \frac{2\pi - \alpha}{\alpha}\right) > 1$, then $I_c := [-I_\alpha; -1/I_\alpha]$ (details about the derivation can be found in [16, Theorem 3.3], [28, Theorem 1]). This gives us

$$-I_\alpha \leq \kappa_\varepsilon \leq -\frac{1}{I_\alpha} \quad \Longleftrightarrow \quad \frac{\omega_p}{\sqrt{I_\alpha \varepsilon_d + \varepsilon_\infty}} \leq \omega \leq \frac{\omega_p}{\sqrt{\varepsilon_\infty + \frac{\varepsilon_d}{I_\alpha}}},$$

$$I_\omega := \left[\frac{\omega_p}{\sqrt{I_\alpha \varepsilon_d + \varepsilon_\infty}}; \frac{\omega_p}{\sqrt{\varepsilon_\infty + \frac{\varepsilon_d}{I_\alpha}}} \right] \tag{19}$$

Moreover, we have the following result:

- If $\omega \notin \left[\frac{\omega_p}{\sqrt{I_\alpha \varepsilon_d + \varepsilon_\infty}}; \frac{\omega_p}{\sqrt{\varepsilon_\infty + \frac{\varepsilon_d}{I_\alpha}}} \right]$: problem in $\underline{H}_z$ is well-posed in $H^1_{loc}(\mathbb{R}^2)$. Mathematical well-posedness in this function space guarantees to have a bounded total electromagnetic energy.

- If $\omega \in I_\omega \setminus \{\omega_{sp}\}$: problem in $\underline{H}_z$ is ill-posed in $H^1_{loc}(\mathbb{R}^2)$. There exist black-hole waves $s \notin H^1_{loc}(\mathbb{R}^2)$ that propagate towards the corners.

Remark 7. Given a polygonal interface Σ with N corners c_i, $i = 1, \ldots, N$, and denoting α_i, $i = 1, \ldots, N$ all the interior angles in $\mathbb{D}$, one can define subintervals

$$I_{c_i} := [-I_{\alpha_i}; -1/I_{\alpha_i}], \text{ and } I_{c_i} \subseteq I_c, i = 1, \ldots N, \text{ or equivalently } I_{\omega_i} \subseteq I_\omega, i = 1, \ldots N.$$

This means that, depending on the contrast κ_ε (and therefore depending on the angular frequency ω), all black-hole waves, or only some of them, can be excited. This will play a certain role when interpreting numerical results.

Remark 8. Black-hole waves can be characterized as follows. Given a corner c, we denote (r, θ) the polar coordinates centered at c, the black-hole wave propagating towards the corner c is of the form $s(r, \theta) = r^{i\lambda} \Phi(\theta)$, with $\lambda \in \mathbb{R}^*$, and Φ a periodic function. Moreover it has been established that (see [20] for details):

---

[5] One can also define C_{ext}, the extinction cross section as $C_{ext} = C_{abs} + C_{sca}$. It will not be used in this work.
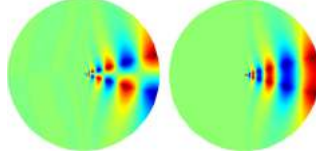
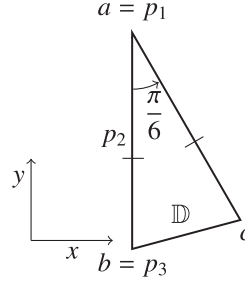**Fig. 1.** Representation of black-hole waves near a corner: odd (left), and even (right).

Fig. 2. Physical domain and notations. 2D section in the (x, y)-plane of the metallic rod.

- If $\omega \in \left[\dfrac{\omega_p}{\sqrt{I_\alpha \varepsilon_d + \varepsilon_\infty}}, \omega_{sp} \right)$, the black-hole wave is *an odd coupled plasmon*. This means that the black-hole wave exhibits two localized oscillating behaviors along the interface that are skew-symmetric with respect to the angle's bisector (Φ is an odd function).

- If $\omega \in \left(\omega_{sp}, \dfrac{\omega_p}{\sqrt{\varepsilon_\infty + \frac{\varepsilon_d}{I_\alpha}}} \right]$, the black-hole wave is *an even coupled plasmon*. This means that the black-hole wave exhibits two localized oscillating behaviors along the interface that are symmetric with respect to the angle's bisector (Φ is an even function).

Fig. 1 represents the two types of black-hole waves near a corner.

Remark 9. The specific case $\omega = \omega_{sp}$ is strongly ill-posed, the provided black-hole characterization is valid for $\omega \in I_\omega \setminus \{\omega_{sp}\}$. We refer for example to [15,19,29] for more details.

The two-dimensional case is fully characterized in frequency-domain. It provides the adequate framework to investigate if the limiting amplitude principle holds in plasmonic structures. In particular, we will look for a signature of this critical interval I_ω in time-domain.

3.2. Physical problem

In order to investigate situations with corners, we choose an isosceles triangle of upper aperture $\frac{\pi}{6}$, with characteristic size (height of longest bisector) equal to 20 nm for the transversal section $\mathbb{D}$ (see Fig. 2) and with area $a_T \approx 1.07 \times 10^{-16}$ m^2. It is tilted so that the edge ab is vertical.

The exterior domain $\mathbb{R}^2 \setminus \bar{\mathbb{D}}$ is filled with vacuum ($\varepsilon_d = 1$). The section $\mathbb{D}$ will either consist of

(i) Dielectric: $\varepsilon_\infty = 3.73$, $\omega_p = 0$ rad s^{-1}.
(ii) Gold: $\varepsilon_\infty = 1$, $\omega_p = 13.87 \times 10^{15}$ rad s^{-1}, with values taken from [30].
(iii) Another Drude material: $\varepsilon_\infty = 3.7362$, $\omega_p = 13.87 \times 10^{15}$ rad s^{-1}.

We will illuminate the structure at a range of pulsations $[\omega_{min}, \omega_{max}]$ that includes the critical interval I_ω associated to both materials[6] and that is such that $\omega_{max} \leq \omega_p$. Therefore the smallest wavelength is greater than

---

[6] Here, if $\tilde{\omega} \in I_\omega$, then $\tilde{\omega} \leq \dfrac{\omega_p}{\sqrt{\varepsilon_\infty + \frac{\varepsilon_d}{I_\alpha}}} \leq \omega_p$.

$\frac{2\pi c_0}{\omega_p} \approx 135$ nm, with $c_0 = \frac{1}{\sqrt{\varepsilon_0 \varepsilon_d \mu_0}}$. In this regard, the metallic structure is subwavelength for incident illuminations below the plasma angular frequency ω_p.

Some quantities will be visualized at three selected probe points: p_1 situated at the top vertex a, p_2 is the middle of segment $[ab]$ and p_3 situated at the left bottom vertex b. To investigate the limiting amplitude principle, we use an incident illumination $(\underline{\vec{E}}_{\perp,inc}, \underline{H}_{z,inc})$ (added to radiation conditions). The latter will be

  (a) a monochromatic plane wave (solution of Maxwell's in vacuum), or
  (b) a polychromatic Gaussian pulse (Gaussian modulated plane wave).

We choose the vertical direction of propagation $-y$ for the incident plane wave field. By tilting the triangle, we break the symmetry, allowing us to excite both odd and even coupled plasmons.

3.3. Limiting amplitude principle requirements

The monochromatic case (a) is readily covered by the limiting amplitude principle framework. Indeed, as already mentioned in Remark 2, the total electromagnetic field can then be decomposed into the incident contribution $(\underline{\vec{E}}_{inc,\perp}, \underline{H}_{inc,z})$ and the scattered one $(\underline{\vec{E}}_{sca,\perp}, \underline{H}_{sca,z})$. As a result, the scattered field $(\underline{\vec{E}}_{sca,\perp}, \underline{H}_{sca,z})$ verifies Maxwell's equations with homogeneous radiation conditions and source term $\underline{\vec{J}}_{ext,\perp}$ with support in $\mathbb{D}$. This source term expresses the fact that the incident plane wave $(\underline{\vec{E}}_{inc,\perp}, \underline{H}_{inc,z})$ is solution of Maxwell's equation in vacuum, but is not solution in the scatterer. Since the incident field is monochromatic, so is the source term. In other words, our source term is monochromatic, with support $\Subset \mathbb{R}^2$ and in $L^2(\mathbb{R}^2)$ which fits in the theoretical framework led by [11,12] to investigate the limiting amplitude principle.

Same procedure can be applied with the Gaussian modulated plane wave (b). However, in this case, the resulting source term $\underline{\vec{J}}_{ext,\perp}$ in the scattered field equation is not monochromatic anymore. The latter is in addition attenuated. This case does not readily fall into the limiting amplitude principle framework. However, such an incident field allows for the excitation of the scatterer by a whole range of pulsations using one single excitation. Moreover, using Fourier transform, the spectral response of the scatterer is easily attainable once the time-domain fields are known. Source (b) provides a practical (but empirical) approach to investigate the problem.

3.4. Numerical framework and strategy

In what follows, we will need to compute a numerical approximation of the solution of the time-domain equations. To do so, we consider a Discontinuous Galerkin Time Domain (DGTD) framework as developed in [31]. This numerical framework is particularly adapted to the challenges encountered for scattering problems and has been assessed on several occasions especially for plasmonic problems (see *e.g.* [32,33] and references therein). In the numerical tests, we use a non-dissipative DGTD scheme for the whole system with unknowns $(\mathbf{E}, \mathbf{H}, \mathbf{J})$. It relies on a discontinuous Galerkin finite element space discretization (with Lagrange nodal basis) with centered fluxes, and a leap-frog scheme in time. This scheme has the advantage to be explicit; the price to pay is that one should choose discretization parameters according to a CFL constraint. Computations are made on an adimensionalized version of the system, quantities plotted later in the paper have been re-dimensionalized.

We approximate the solution over a sufficiently long physical time T relative to the period of the incident signal: T represents 100 to 200 times the period of the monochromatic source (a), or the period of the smallest frequency in the pulse of the polychromatic source (b). This time has been empirically adjusted so that it does not affect our conclusions with regards to the convergence of the computed quantities. We are able to compute all the quantities mentioned in Section 2: time evolution of the energy, time evolution of the fields at probe points, and time averaged quantities. In particular, we compute the discrete time evolution of the total discrete energy (on the whole computational domain) and in a small domain surrounding each corner. When considering a polychromatic source (b), we compute cross sections and Poynting fluxes at the end of the simulation, using a Fourier transform that is computed "on the fly" (done in one simulation run). For illuminations considered in this work, the quantity $|\underline{\vec{\Pi}}_{inc}|$ that appears in (18) can be computed analytically.

As mentioned previously, the monochromatic source type (a) falls into the exact limiting amplitude principle setting, and therefore will be used to find a clear indication of a non-harmonic response to the harmonic incident field. The polychromatic source type (b) will allow to obtain a spectral response and investigate physical quantities
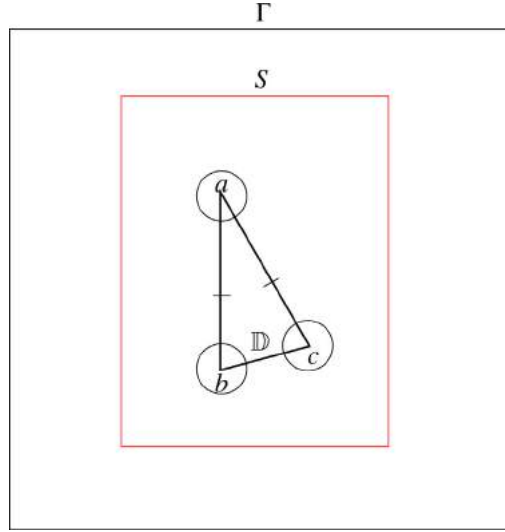
Fig. 3. The computational domain is delimited by an artificial boundary Γ. A side of Γ has a length of 60 nm. The cross sections are computed on a line S around the scatterer, which is approximately 20 nm away from it. The black-hole fluxes and energy are computed in small disks centered at each corner.

over the whole spectral band of interest, and in one single run. The two approaches are thus complementary and are used to thoroughly test our approach.

The scheme has been implemented in a in house 2D Fortran code developed within the Inria Atlantis project team (Inria Sophia Antipolis, France).[7] Previous versions of this code have been already exploited in the context of [34] and [35]. Discretization parameters have been fixed so that we use a discretization fine enough with respect to the incident wavelength and fulfill the CFL condition. If Δt denotes the physical time step, and h_{max} the space discretization parameter, we use $\Delta t \approx 10^{-19}$s and $h_{max} \approx 1$ nm (the mesh is non uniform and is appropriately refined at the corners of the domain and close to the interface, where the size of the mesh is approximately $\frac{1}{5}h_{max}$). Unless specified, we use a $\mathbb{P}_2$ (polynomials of degree less than or equal to 2) basis for our finite element space. Finally, in Fig. 3 we detail the *computational domain* and geometrical entities that we use to compute the solution and quantities of interest. Numerically, one computes Poynting fluxes, called *black-hole fluxes* for short, around each corner, for ω in the range of pulsations of interest:

$$F_k(\omega) := \int_{D_k} \operatorname{div}\underline{\Pi}(\omega)d\mathbf{x}, \quad k = \{a, b, c\}, \tag{20}$$

where $(D_k)_{k=\{a,b,c\}}$ are (small) disks of radius 2 nm around each corner a, b, c, respectively. Similarly, the energies at the vicinity of each corner are computed for $k = \{a, b, c\}$ and $t \in [0, T]$ using

$$\mathcal{E}_k(t) = \frac{1}{2}\|\sqrt{\varepsilon_0\varepsilon_r}\vec{E}_\perp(t)\|^2_{L^2(D_k)} + \frac{1}{2}\|\sqrt{\mu_0}H_z(t)\|^2_{L^2(D_k)} + \frac{1}{2\varepsilon_0\omega_p^2}\|\vec{J}_\perp(t)\|^2_{L^2(D_k)}. \tag{21}$$

4. Numerical results

First, we investigate the situation where the limiting amplitude principle (LAP) holds. This is the situation where one considers for example a dielectric inclusion (case (i) in Section 3.2). We use this simple case as a benchmark to validate our strategy. Then, we consider situations where the LAP might not hold (cases (ii) and (iii) in Section 3.2).

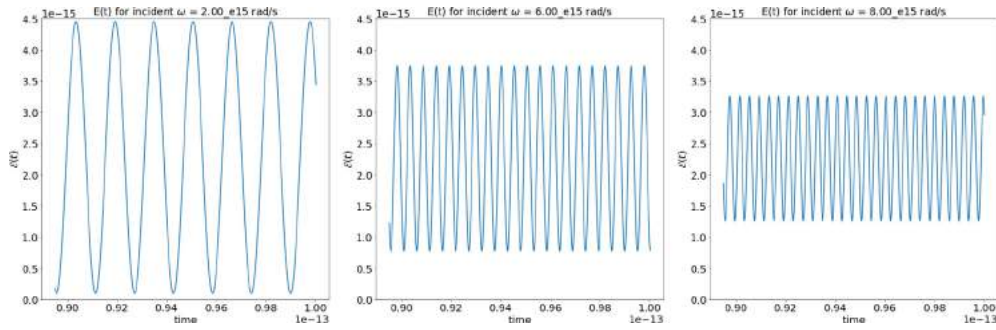[7] http://www-sop.inria.fr/atlantis/.

Fig. 4. Representation of $\mathcal{E}(t)$ (computed via (6)) for different incident fields. The incident field is monochromatic, we vary the pulsation ω and represent the result for $\omega = 2 \times 10^{15}$ rad s^{-1}, $\omega = 6 \times 10^{15}$ rad s^{-1}, $\omega = 8 \times 10^{15}$ rad s^{-1}.
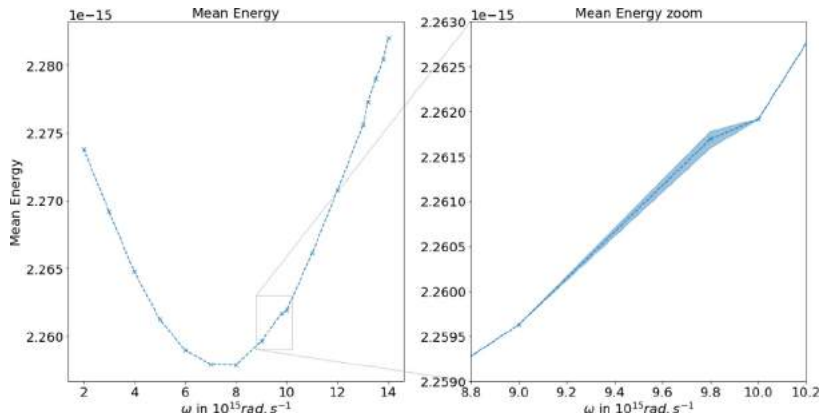

Fig. 5. (Left) Mean energy $\underline{\mathcal{E}}$ (computed with (15)) with respect to the incident pulsation. For each value of the pulsation ω, we compute the mean of the energy on different time intervals of length $T(\omega)$ over the simulation time duration. (Right) Zoom of the energy mean where there is a maximum of variations, scaled by a factor 10. Computations show relative variations of order 10^{-6}.

4.1. When the limiting amplitude principle holds

We consider here case (i), of a dielectric inclusion.[8]

4.1.1. Response to monochromatic illumination.

We consider a monochromatic incident field (a) of pulsation ω, with $\omega \in [2 \times 10^{15}, 13.8 \times 10^{15}]$ rad s^{-1}.

Study of the energy. Fig. 4 represents the evolution of the electromagnetic energy $\mathcal{E}$ over the last 10% of the total physical time i.e. $t \in [0.9T, T]$, for some incident pulsations ω. Results show that the electromagnetic energy stays clearly bounded over time and is periodic. Moreover, for each pulsation, we observe that the value of the energy mean $\underline{\mathcal{E}}$ (see Fig. 5) varies in the range $[2.255 \times 10^{-15}, 2.285 \times 10^{-15}]$. Thus, it stays of the same order of magnitude over pulsations and varies fairly little (relative variation of $\approx 1\%$).

In the spirit of Remark 6, at each fixed pulsation ω, we compute the mean value of the energy over several time intervals of length $T(\omega)$ (these intervals are chosen around the end of the physical simulation time). We observe only relative variations of maximum 10^{-6}, that allows us to conclude that (for a fixed pulsation) the mean value of the energy is numerically independent of the chosen interval: the signal appears to be harmonic at the expected frequency.

---

[8] To be complete, and for a further validation of the benchmark, the very simple case of vacuum has also been tested. The results are conclusive and as expected. We choose not to reproduce them here, since the situation is completely straightforward. The results will be only used sometimes for comparison, to support our reasoning.
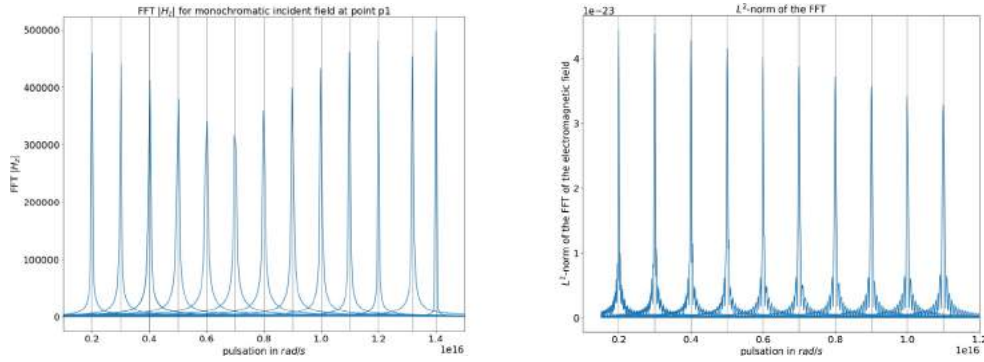
Fig. 6. Left: FFT of H_z at first probe points p_1. Similar plots are obtained at other probe points and we do not represent them here to ease the reading. Right: L^2-norm of the FFT of the total electromagnetic field on the whole computational domain. Vertical lines represent the chosen incident ω. All obtained peaks match the incident pulsation.

Table 1
Relative errors of the computed main pulsations at the chosen probe points (via FFT) with the exact pulsation ω, with $\omega \in [2 \times 10^{15}, 12 \times 10^{15}]$ rad s^{-1}.

ω (rad s^{-1})	Error p_1	Error p_2	Error p_3
2e15	4.61e−3	4.61e−3	4.61e−3
4e15	4.61e−3	4.61e−3	4.61e−3
6e15	4.61e−3	4.61e−3	4.61e−3
8e15	3.23e−3	3.23e−3	3.23e−3
10e15	1.66e−3	1.66e−3	1.66e−3
12e15	6.17e−4	6.17e−4	6.17e−4

Fourier transform. We now compute the Fourier transform (via FFT) of the magnetic field over the range of frequencies of interest at chosen probe points (see Section 3.2), and compute the relative error between the computed main pulsation and the chosen incident pulsation ω. Fig. 6 (Left) and Table 1 show that we recover harmonic signals centered within less than 0.4% of relative error from the incident pulsation. To observe whether these effects are also visible globally, we also plot in Fig. 6 (right) the L^2-norm in space of the Fourier transform (in time) of the total electromagnetic field. Here again, we recover a (numerical) harmonic behavior. The above observations can be viewed as strong numerical evidences that the limiting amplitude principle holds, as expected for dielectric materials.

4.1.2. Response to polychromatic illumination

We also investigate the FFT of the magnetic field for a polychromatic illumination. We choose here to represent the field H_z since this is the field that naturally compares to frequency-domain approach via Eq. (11a), but we could have also represented the two components of the electric fields (leading to similar conclusions). This allows to: (i) alleviate any discrepancy in the Fourier signal that may be sensitive to a single pulsation, (ii) test multiple incident pulsations in one single run. Fig. 7 represents the FFT of the magnetic field at probe points in the case of propagation of a polychromatic pulse (b). Results show that a Gaussian Fourier signal is recovered without any discrepancy. Same conclusion holds for the global L^2-norm of the Fourier transform, that we do not reproduce here.

4.2. Breaking the limiting amplitude principle

We now consider a metallic scatterer with parameters from case (ii) or (iii). We will follow the same strategy as in Section 4.1, but first we make use of results from Section 3.1.
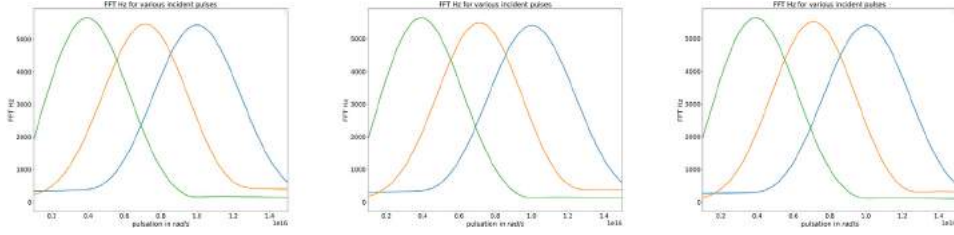
Fig. 7. Modulus of the Fourier transform for various Gaussian pulses at probe points p_1 (left), p_2 (middle), p_3 (right) for several Gaussian pulses. We use several central frequencies (4×10^{15}, 7×10^{15} and 10×10^{15} rad s^{-1}).

4.2.1. Explicit critical interval of pulsations

In this section we specify I_ω given in (19) for cases (ii) and (iii). Given the geometry, the critical interval is associated to corner a with aperture $\frac{\pi}{6}$ (then $I_\alpha = 11$). Using Remark 7 we compute the critical subintervals associated to the other corners b, c to identify when black-hole waves may appear.

- For material (ii) (corresponding to gold) we obtain

$$\omega \in I_\omega \quad \Longleftrightarrow \quad \frac{\omega_p}{\sqrt{12}} \leq \omega \leq \frac{\omega_p}{\sqrt{\frac{12}{11}}}$$

  leading to $I_\omega = [4.0039 \times 10^{15}, 13.2795 \times 10^{15}]$ rad s^{-1}, and the surface plasmon angular frequency (13) is equal to

$$\omega_{sp} := \frac{\omega_p}{\sqrt{2}} \simeq 9.8076 \times 10^{15} \text{ rad } s^{-1}.$$

  The other two corners b, c of angle $\frac{5\pi}{12}$, provide $I_{\omega_b} = I_{\omega_c} = [6.3307 \times 10^{15}, 12.3409 \times 10^{15}]$ rad s^{-1}.

- For material (iii) we obtain

$$\omega \in I_\omega \quad \Longleftrightarrow \quad \frac{\omega_p}{\sqrt{11 + 3.7362}} \leq \omega \leq \frac{\omega_p}{\sqrt{3.7362 + \frac{1}{11}}}$$

  leading to $I_\omega = [3.6131 \times 10^{15}, 7.0899 \times 10^{15}]$ rad s^{-1}, and the surface plasmon angular frequency (13) is equal to

$$\omega_{sp} := \frac{\omega_p}{\sqrt{1 + 3.7362}} \simeq 6.3732 \times 10^{15} \text{rad s}^{-1}.$$

  Further we obtain $I_{\omega_b} = I_{\omega_c} = [5.0524 \times 10^{15}, 6.9355 \times 10^{15}]$ rad s^{-1}.

Remark 10. In what follows, we will indicate I_ω in light red, and the subinterval I_{ω_b} in dark red in the plots.

4.2.2. Response to monochromatic illumination

We consider a monochromatic incident field of pulsation ω, with $\omega \in [2 \times 10^{15}, 13.8 \times 10^{15}]$ rad s^{-1}. The covered pulsation range includes the critical interval I_ω associated to both materials. Contrary to the previous case we expect changes for $\omega \in I_\omega$.

Study of the energy. Fig. 8 represents the evolution of the energy for several incident pulsation values for both cases. Contrary to the previous case, we observe a drastic change of behavior of the energy when the pulsation ω of the monochromatic source belongs to I_ω: the energy drastically increases by several orders of magnitude (10^{-13} compared to 10^{-15}), and does not exhibit a clear periodic behavior. This change is clearly visible when ω "enters" the critical interval. Moreover, at lower pulsations, the energy exhibits a periodic behavior. When ω "leaves" the critical interval, the energy drastically decreases. For case (ii) it is not clear that we recover a periodic signal at the chosen pulsation (located right outside of the critical interval), however for case (iii) the periodic behavior for $\omega \notin I_\omega$ is more visible. Fig. 9 represents the means of energy $\underline{\mathcal{E}}$ with respect to the monochromatic pulsation. For each incident source, we compute the mean of the energy for different time intervals of length $T(\omega)$ over the final
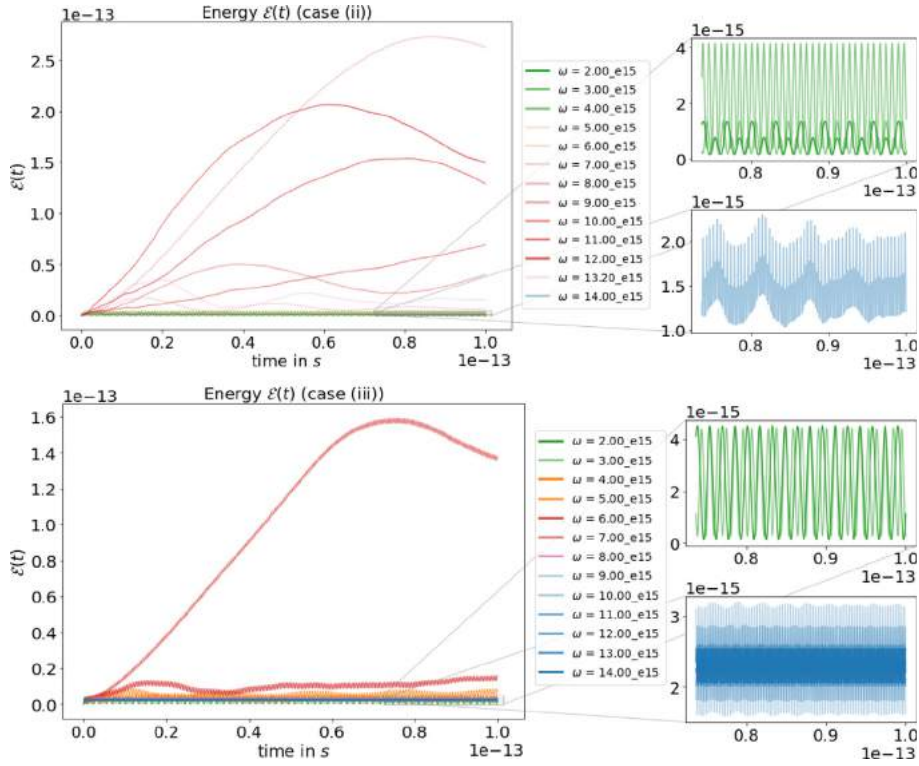
Fig. 8. Representation of $\mathcal{E}(t)$ (computed via (6)) for different incident fields for case (ii) (top) and for case (iii) (bottom), with zooms at the long time simulation. The green and blue curves correspond to $\omega \notin I_\omega$, whereas the warm colored curves correspond to $\omega \in I_\omega$. (For interpretation of the references to color in this figure legend, the reader is referred to the web version of this article.)

part of the simulation time duration. The light blue shadow indicates the variations between those computations (we report the minimal and maximal values), scaled by a factor 10. As observed before, the energy is considerably more important at critical pulsations (indicated by the red zones). Additionally the computation of the mean $\underline{\mathcal{E}}$ is highly sensitive to the time interval when we choose $\omega \in I_\omega$, indicating that a periodic regime may not be established. Note that the energy mean is two orders of magnitude stronger than what was observed in Section 4.1. Furthermore, one can observe that the strongest variations within the means are obtained when all corners are excited ($\omega \in I_{\omega_b}$). Based on the energy observations, one can conclude that there is definitely a change of behavior at critical pulsations, indicating that the limiting amplitude principle should not hold.

Fourier transform at probe points. Fig. 10 represents the Fourier transform of the magnetic field over the range of frequencies of interest at probe point p_1 (see Section 3.2). Similar plots have been obtained for other probe points, we do not present them here. Fig. 11 represents the L^2-norm in space of the Fourier transform (in time) of the whole electromagnetic field ($\vec{E}_\perp$, H_z).

Results show that we still recover harmonic-like signals centered at the incident pulsation, however the signal is perturbed for critical pulsations. We can make several observations:

- at each frequency, one main peak occurs at the pulsation of the incident field. The numerical relative error to the exact value does not exceed the one obtained in Section 4.1,
- for some pulsations inside the critical interval, the main peak is wider and/or stronger in intensity,
- for pulsations inside the critical subinterval, secondary peaks do appear.

The last two items above invalidate the limiting amplitude principle.

In the next section we compute the Fourier transform when considering a Gaussian pulse, where the break of the harmonic signal is significantly more striking.
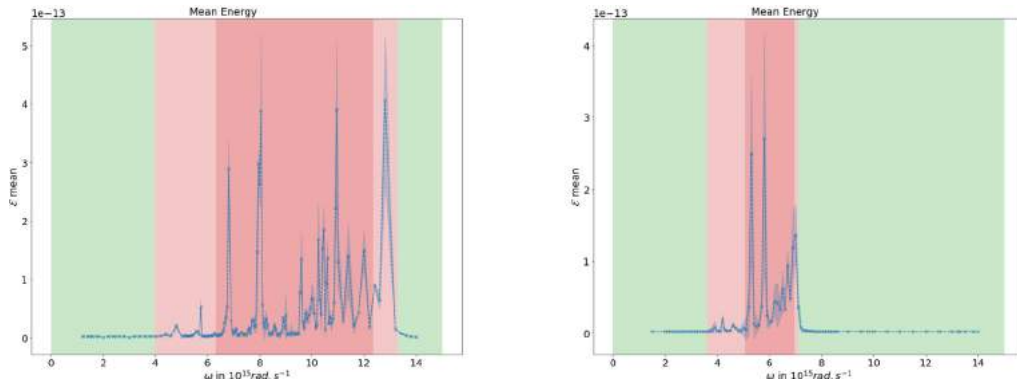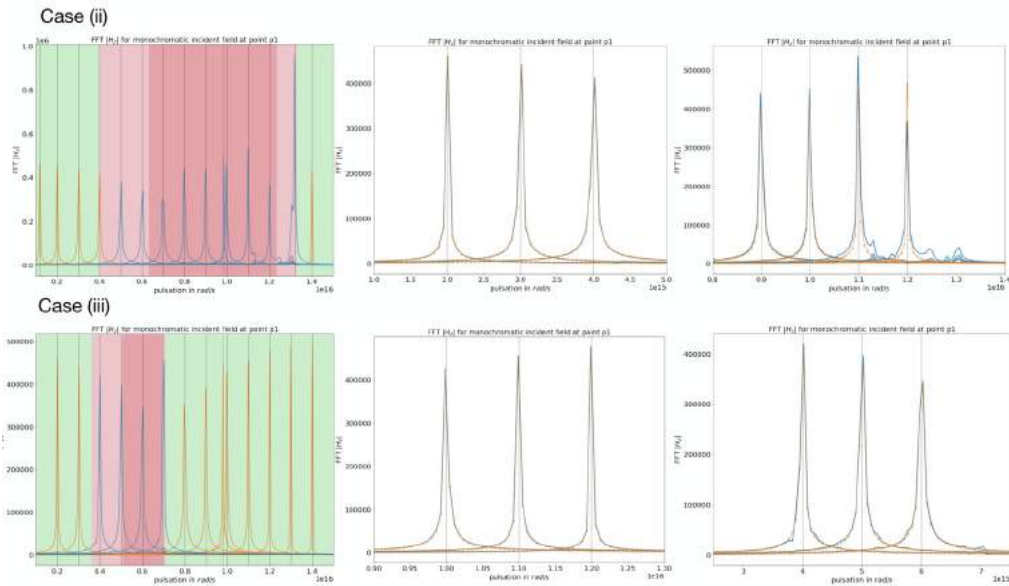
Fig. 9. Mean of energy $\underline{\mathcal{E}}$ (computed with (15)) with respect to the monochromatic pulsation: for case (ii) (left), for case (iii) (right). The green zones indicate when $\omega \notin I_\omega$, the red zones indicate when $\omega \in I_\omega$. The darker red zone indicates the critical subinterval $\omega \in I_{\omega_b}$. (For interpretation of the references to color in this figure legend, the reader is referred to the web version of this article.)

Fig. 10. (Left) FFT of H_z at first probe point p_1: for case (ii) (top row), for case (iii) (bottom row). Vertical lines represent the chosen ω. The green zones indicate when $\omega \notin I_\omega$, the red zones indicate when $\omega \in I_\omega$. The darker red zone indicates the critical subinterval $\omega \in I_{\omega_b}$. (Middle, Right): samples of FFT from the two cases: for $\omega \notin I_\omega$ (middle), and for $\omega \in I_\omega$ (right). The orange '$-\times$' curves correspond to FFT peaks in vacuum (where the response is always harmonic). (For interpretation of the references to color in this figure legend, the reader is referred to the web version of this article.)

4.2.3. Response to polychromatic illumination

We now investigate the response of the metallic scatterer to a pulse illumination (b). As before, we investigate the Fourier transform of the magnetic field.

Fourier transform. Fig. 12 represents the Fourier transform of the magnetic field at the probe points p_1, p_2, p_3 for a Gaussian pulse centered at 4×10^{15}, 7×10^{15} and 10×10^{15} rad s^{-1}. One clearly observes that the Gaussian signal is recovered for $\omega \notin I_\omega$ and completely perturbed when $\omega \in I_\omega$. These effects are also observable globally. In Fig. 13, we plot the L^2-norm (in space) of the Fourier transform of the whole electromagnetic field ($\bar{E}_\perp$, H_z) (we here choose to represent only one central frequency 7×10^{15} rad s^{-1}, the others being similar).
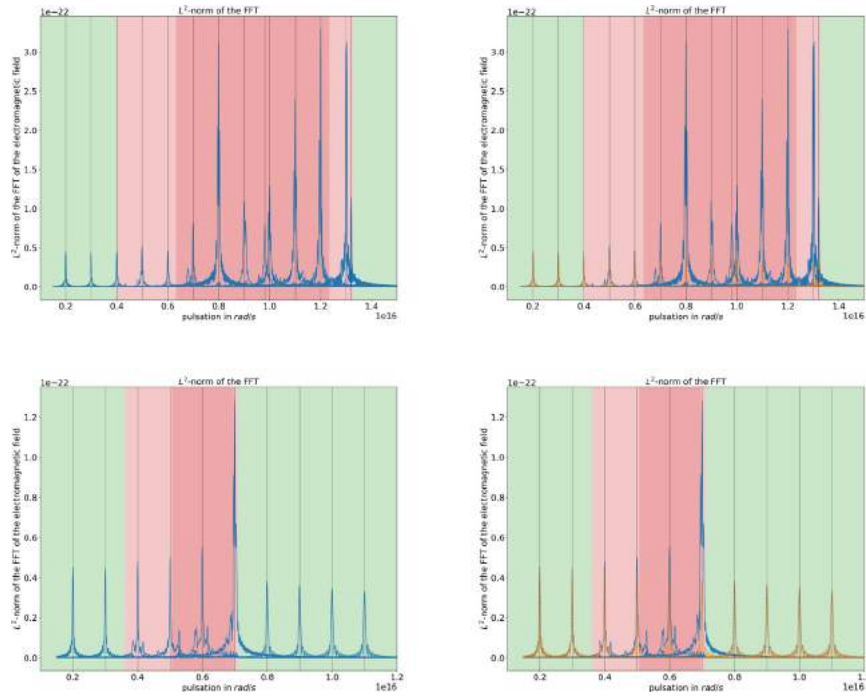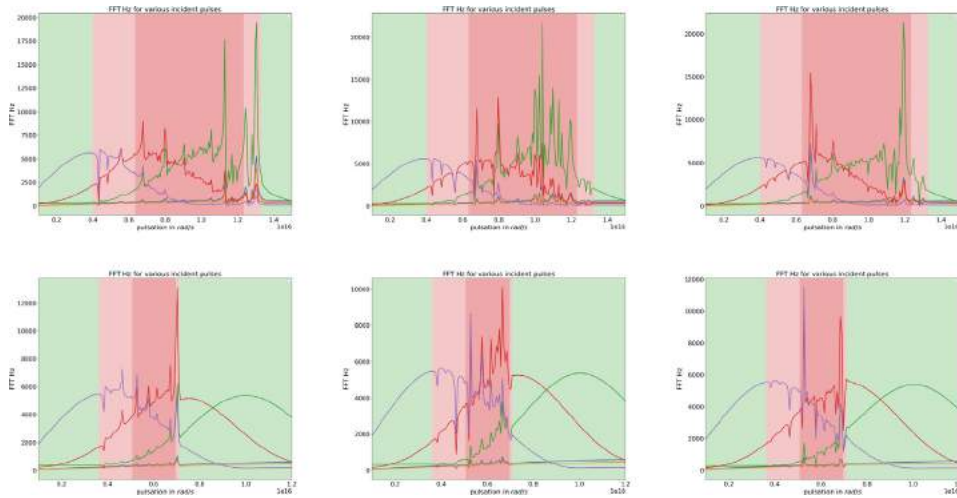
Fig. 11. L^2-norm of FFT of the whole electromagnetic field (left) comparison with vacuum results (right): for case (ii) (top row), for case (iii) (bottom row). The orange '$-\times$' curves correspond to FFT peaks in vacuum and the computations have been performed on same meshes for both cases. Vertical lines represent the chosen ω. The green zones indicate when $\omega \notin I_\omega$, the red zones indicate when $\omega \in I_\omega$. The darker red zone indicates the critical subinterval $\omega \in I_{\omega_b}$. (For interpretation of the references to color in this figure legend, the reader is referred to the web version of this article.)
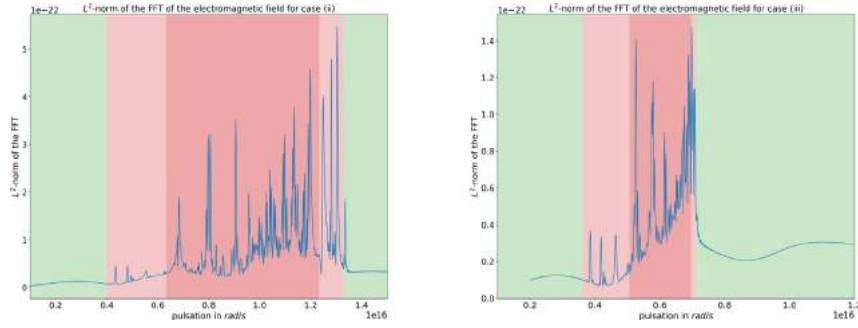

Fig. 12. FFT of $|H_z|$ at probe points p_1 (left), p_2 (middle), p_3 (right) for several Gaussian pulses centered at 4×10^{15}, 7×10^{15} or 10×10^{15} rad s^{-1} and two widths: for case (ii) (top row), for case (iii) (bottom row). The green zones indicate when $\omega \notin I_\omega$, the red zones indicate when $\omega \in I_\omega$. The darker red zone indicates the critical subinterval $\omega \in I_{\omega_b}$. (For interpretation of the references to color in this figure legend, the reader is referred to the web version of this article.)

Fig. 13. L^2-norm in space of the time FFT of the whole electromagnetic field for a Gaussian pulse centered at 7×10^{15} rad s^{-1}: for case (ii) (left), for case (iii) (right). The green zones indicate when $\omega \notin I_\omega$, the red zones indicate when $\omega \in I_\omega$. The darker red zone indicates the critical subinterval $\omega \in I_{\omega_b}$. (For interpretation of the references to color in this figure legend, the reader is referred to the web version of this article.)

4.2.4. Conclusion

To sum up, through various quantities of interests, we can clearly identify a change of behavior in the spectral response in the critical interval. This provides numerical evidences about the proposed limiting amplitude principle conjecture. Moreover, using polychromatic pulse illumination, one is directly able to find precisely traces of the critical interval. In what follows, we continue our investigation and examine the impact of underlying black-hole waves on the time-domain simulations.

5. Black-hole waves resonances

Results from previous sections clearly highlight the break of the limiting amplitude principle for critical pulsations. In this section we investigate its impact on more physical quantities and situations.

5.1. Cross sections and black-hole fluxes

The amount of light diffracted or absorbed by an illuminated tridimensional structure is measured by energy fluxes. The intrinsic capacity of an object to diffract or absorb light is then measured relative to the power of the incident light beam excitation. One way to quantify this is to measure the diffraction or absorption cross sections (defined in (18)). As a matter of fact, these provide the equivalent area of the incident beam that would have to be used to obtain the same energy than that provided by the illuminated object. Thus when a scatterer absorbs or scatters light on a much larger area compared to its physical size, it transpires in the absorption and scattering cross sections as intense peaks, and their location indicates the associated resonance frequency. Cross sections are by nature positive and in the 2D setting that we consider, cross sections have the dimension of a length and provide an equivalent perimeter. We now investigate how they vary for cases (ii) and (iii), in the context of a polychromatic illumination.

Remark 11. We choose a polychromatic source that illuminates the range of interest $[1 \times 10^{15}, 14 \times 10^{15}]$ rad s^{-1}. With these chosen parameters, the range of frequencies at which we illuminate the structure lies in the visible-near UV range. Furthermore, as mentioned in Section 3.2, the structure used is subwavelength.

Cross sections. Fig. 14 represents the scattering and absorption cross sections obtained with an incident Gaussian pulse for both Drude materials. It must be emphasized that our interest lies more in finding a clear trace of the critical interval than in extracting a precise position of resonances. Indeed, results show a clear trace of the critical interval: strong resonances do appear for $\omega \in I_\omega$. While C_{sca} remains positive, C_{abs} presents quite significant unphysical oscillations and negative values. We observe that the latter is also sensitive to mesh discretization and the chosen degree of interpolation (even for a refined mesh).

These observations can be explained. Scattering cross section C_{sca} tracks the far-field's response whereas absorption cross section C_{abs} is linked to the near-field's response of the scatterer. The more erratic behavior of
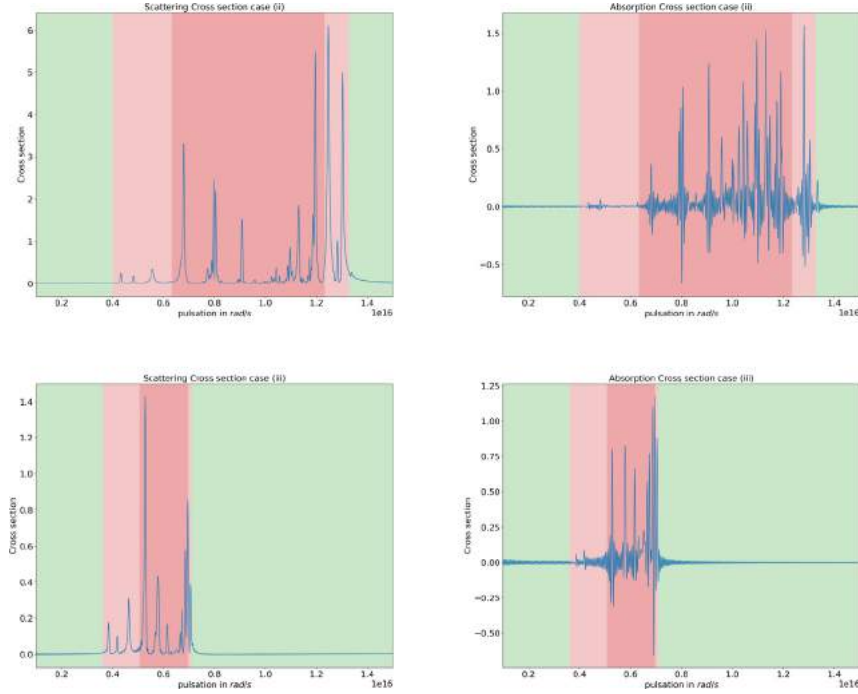
Fig. 14. (Left): Scattering cross sections C_{sca} (computed with (18)) when considering a Gaussian pulse: for case (ii) (top row), for case (iii) (bottom row). (Right): Absorption cross sections C_{abs} when considering a Gaussian pulse: for case (ii) (top row), for case (iii) (bottom row).

C_{abs} can thus be explained by the difficulties to accurately capture black-hole waves close to the corners, where discretization has to be fine enough to avoid spurious reflections. This phenomenon has been well characterized in frequency-domain [20], where an efficient modified finite element method (FEM) approximation with corner treatments has been developed. Results may indicate that, even for time-domain formulations for which the problem is mathematically well-posed, the discretization fails to approximate those highly-oscillatory behaviors and would benefit from a similar specific corner treatment. This will be part of future investigations. As mentioned before, while the polychromatic illumination does not fit the theoretical LAP framework, it allows to highlight the predicted phenomena in a single run. This strongly suggests a systematic strategy to numerically identify signatures of a critical interval on a given structure, even when the theory is not known.

Poynting fluxes. Fig. 15 compares the total Poynting flux to the black-hole fluxes around each corner of the triangle scatterer. The black-hole fluxes $(F_k)_{k=\{a,b,c\}}$ are computed in a disk centered at the corner and of radius 2 nm, see (20) and Fig. 3 for details.

Results show that:

(i) all black-hole fluxes are (almost) equal to zero when $\omega \notin I_\omega$ (no black-hole waves are excited);

(ii) black-hole fluxes remain small when $\omega \in I_\omega \setminus I_{\omega_b}$, that is when only the black-hole singularities located at the corner a can be excited;

(iii) all black-hole fluxes are significant when $\omega \in I_{\omega_b}$ (corresponding to all black-hole singularities being excited); in this situation, we also observe that almost all the contributions to the Poynting flux are due to the corners.

All those observations are in accordance with theory from frequency-domain detailed in [20]: this is closely related to black-hole excitation.

All results above illustrate that strong responses arise when illuminating a polygonal metallic obstacle with a source swiping critical pulsations ω, and those strong behaviors are directly connected to the black-hole waves that are known to exist in frequency-domain. Here we considered an *ideal* case without dissipation. In what follows we compare results with and without dissipation: this allows to identify whether the above observations are degenerate
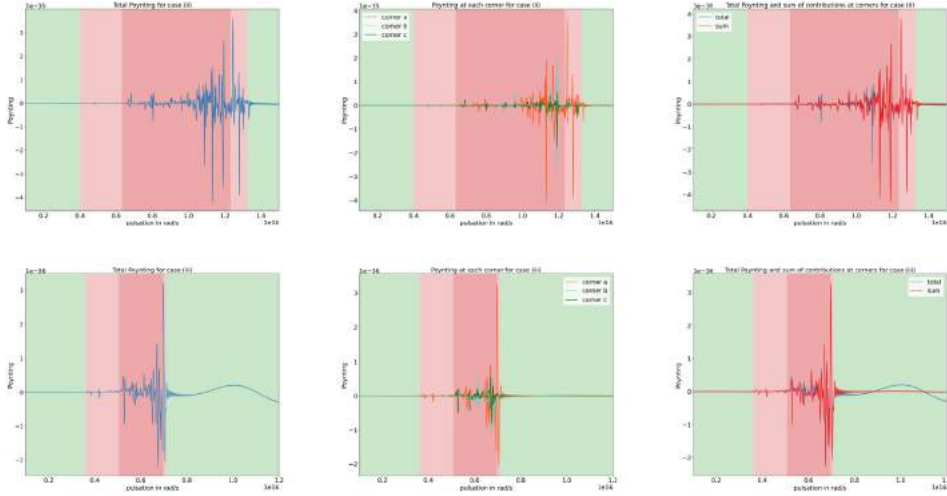
Fig. 15. Poynting fluxes when considering a Gaussian pulse illumination, for case (ii) (top row) and for case (iii) (bottom row). We compute the total Poynting flux (left column), the black-hole fluxes (middle column), and compare the total Poynting flux to the sum of the black-hole fluxes (right column).

behaviors (i.e. they only occur in the absence of dissipation), or intrinsic behaviors (i.e. they are observable also with dissipation), of the physical structure.

5.2. Back to physics: the role of dissipation

Metals are always lossy, meaning that in practice one considers $\gamma \neq 0$ in Eq. (4d). In this section we study the impact of introducing dissipation ($\gamma \neq 0$) in our computations. Note that adding dissipation changes the asymptotics of the solution since the solution will be damped (up to vanishing). Moreover, problem (9) in frequency-domain is always mathematically well-posed in presence of dissipation. This implies that there are actually no critical pulsations to consider. We explore the question of finding a signature of the limit problem (and consequently limit behaviors) in lossy cases.

Figs. 16 and 17 present comparisons between previous cross sections and Poynting fluxes, and the ones obtained when we add dissipation: we now consider models (ii) and (iii) with the physical value $\gamma = 4.515 \times 10^{13}$ rad s^{-1}. Obtained cross sections for lossy cases remain positive (which is more physically relevant) and less sensitive to the mesh discretization. However in both configurations (non lossy, lossy), cross sections present similar behaviors: strong resonances arise at "critical" pulsations. Those resonances have less intensity with dissipation, and dissipation prevents strong spurious resonances mentioned above in the non lossy case (assuming the mesh is sufficiently refined at the corners). The fact that intense resonance peaks remain can be explained via the frequency-domain framework [20,36]. By adding dissipation, the frequency problem becomes well-posed, however strong oscillations at the corners remain. Dissipation allows to *attenuate the black-hole waves*, $s \notin H^1_{\mathrm{loc}}(\mathbb{R}^2)$ being replaced by $s^\gamma \in H^1_{\mathrm{loc}}(\mathbb{R}^2)$, and selects the *outgoing* ones (limiting absorption principle), where the outgoing wave is the one traveling towards the corners (as reference to their names). Observed peaks then correspond to attenuated black-hole waves going towards the corners. Similarly, Poynting fluxes get *smoothed out* by dissipation, and most of the energy fluxes come from the corners at critical pulsations: this corresponds to *attenuated* black-hole resonances contributions.

Remark 12. As explained in Section 3.1, the frequency theory also allows to characterize the singularities as odd or even coupled plasmons depending on the surface plasmon frequency. Due to the chosen non symmetric configuration, we expect that the excitation of odd plasmons will be favored under the surface plasmon frequency, whereas the excitation of even plasmons will be favored above the surface plasmon frequency. One can identify a change of behavior in C_{sca}, where the scattering cross section vanishes for $\omega = \omega_{sp}$.
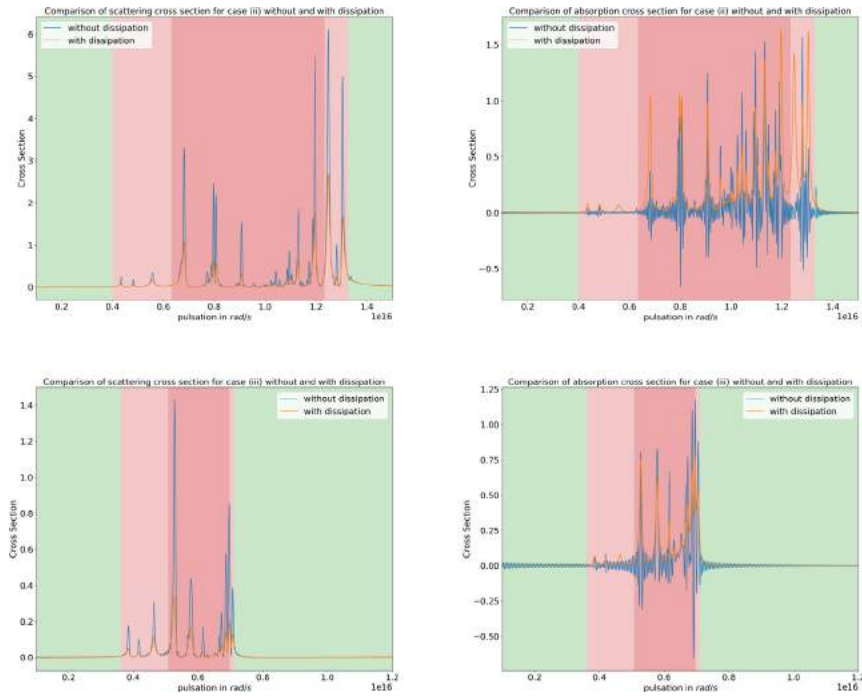
Fig. 16. Comparison of cross sections for cases (ii) (top row) - (iii) (bottom row) with and without dissipation: scattering C_{sca} (left), absorption C_{abs} (right).
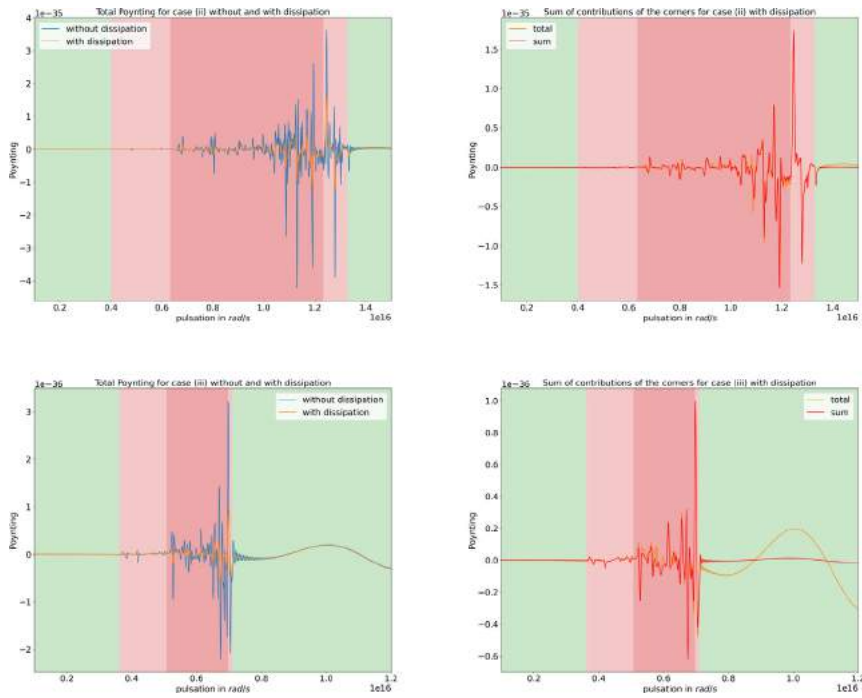

Fig. 17. Left: comparison of Poynting fluxes with and without dissipation: case (ii) (top row), case (iii) (bottom row). Right: comparison of total Poynting fluxes and the sum of the Poynting fluxes at the corners: case (ii) with dissipation (top row), case (iii) with dissipation (bottom row).
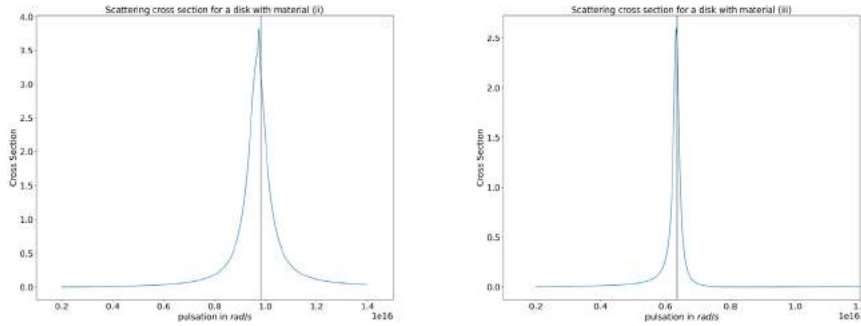
Fig. 18. Scattering cross sections for a disk made of a Drude material (ii) and (iii) (no dissipation). The 2D section of the cylinder (a disk) has the same perimeter as the triangle section used in this work. The maximum is achieved at $\omega = 9.74 \times 10^{15}$ rad s^{-1} for case (ii) (0.6% relative error to ω_{sp}) and $\omega = 6.34 \times 10^{15}$ rad s^{-1} for case (iii) (0.5% relative error to ω_{sp}).
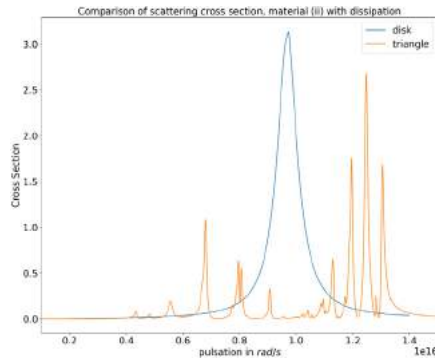

Fig. 19. Comparison of scattering cross sections for a disk made of a Drude material (ii) with dissipation using the triangular section and a disk section with same perimeter as the triangle section.

To sum up, studying the limit non lossy models allows to explain underlying resonances from physical lossy configurations.

5.3. Corner effects

It is well known via Mie theory that dissipative subwavelength cylindrical scatterers exhibit one resonance located at the surface plasmons frequency ω_{sp}. This resonance is called a dipole resonance. This result is in accordance with the fact that the critical interval reduces to exactly $\{\omega_{sp}\}$ for smooth interfaces. We simply provide below illustrations of the above statement, using the same material properties and for $\mathbb{D}$ a disk with same perimeter as the considered triangle. Fig. 18 shows that only one resonance at ω_{sp} is observed. This also allows to additionally validate our approach by recovering a known result.

On the other hand, from Section 5.2 we identify multiple resonances at critical pulsations, and those resonances are related to specific surface plasmons (called in the limit case black-hole waves). In other words, this single subwavelength structure with corners allows to produce multipolar resonances (quadripolar, octopolar, etc...). Furthermore, the level of intensity of these multiple resonances is equivalent to the level of the dipolar resonance that could be obtained with a cylinder with equivalent section perimeter (see Fig. 19). The resonance obtained with a cylinder is however broader. Thus, it is possible to use triangular scatterers rather than circular ones to obtain: (i) multiple resonances with one single structure, (ii) sharper resonances of equivalent intensity than the single dipolar resonance of a cylindrical structure of equivalent perimeter. Polygonal interfaces then offer a larger range of possible light enhancements.

6. Conclusion

In this paper we provided a systematic numerical approach to identify if the limiting amplitude principle holds in ideal plasmonic structures that is, non lossy plasmonic structures with corners, and identified the underlying causes when it does not. Moreover, a study of cross sections and Poynting fluxes revealed that the underlying resonances appearing at critical pulsations are related to localized surface plasmons at the corners called black-hole waves. We found that those characterized behaviors are intrinsic to the problem, as being captured with or without dissipation. Overall, this first work provides an interesting framework to investigate unexplored models and configurations, where no theory is available. One can for example now investigate the fully three-dimensional case, where the associated critical interval is not explicitly known in general, and test other plasmonic models such as Drude–Lorentz or more generalized models (such as those in [31]). In particular, future work will include the study of non-local effects.

Declaration of competing interest

The authors declare that they have no known competing financial interests or personal relationships that could have appeared to influence the work reported in this paper.

Acknowledgment

References

[1] S. Maier, Plasmonics - Fundamentals and Applications, Springer, 2007.

[2] W. Barnes, A. Dereux, T. Ebbesen, Surface plasmon subwavelength optics, Nature 424 (6950) (2003) 824–830.

[3] A. Zayats, I. Smolyaninov, A. Maradudin, Nano-optics of surface plasmon polaritons, Phys. Rep. 408 (3–4) (2005) 131–314.

[4] T. Sannomiya, C. Hafner, J. Voros, In situ sensing of single binding events by localized surface plasmon resonance, Nano Lett. 8 (10) (2008) 3450–3455.

[5] K. Mayer, S. Lee, H. Liao, B. Rostro, A. Fuentes, P. Scully, C. Nehl, J. Hafner, A label-free immunoassay based upon localized surface plasmon resonance of gold nanorods, ACS Nano 2 (4) (2008) 687–692.

[6] L. Novotny, N. Van Hulst, Antennas for light, Nature Photonics 5 (2) (2011) 83–90.

[7] G. Akselrod, C. Argyropoulos, T. Hoang, C. Ciracì, C. Fang, J. Huang, D. Smith, M. Mikkelsen, Probing the mechanisms of large purcell enhancement in plasmonic nanoantennas, Nature Photon. 8 (11) (2014) 835–840.

[8] P. Drude, Zur elektronentheorie der metalle, Ann. Phys. 306 (1900) 566–613.

[9] C. Morawetz, The limiting amplitude principle, Comm. Pure Appl. Math. 15 (1962) 349–361.

[10] N. Iwasaki, On the principle of limiting amplitude, Publ. Res. Inst. Math. Sci. 3 (1968) 373–392.

[11] D. Eidus, The principle of Limit amplitude, Russ. Math. Surv. 24 (1969) 97–167.

[12] G. Kriegsmann, Exploiting the limiting amplitude principle to numerically solve scattering problems, Wave Motion 4 (1982) 371–380.

[13] G. Roach, B. Zhang, The limiting-amplitude principle for the wave propagation problem with two unbounded media, Math. Proc. Camp. Phil. Soc. 112 (1992) 207–223.

[14] B. Gralak, A. Tip, Macroscopic Maxwell's equations and negative index materials, J. Math. Phys. 5 (2010) 052902.

[15] M. Cassier, Analysis of two wave propagation phenomena: 1) space–time focusing in acoustics; 2) transmission between a dielectric and a metamaterial, (Ph.D. thesis), École Polytechnique, 2014.

[16] A.-S. Bonnet-Ben Dhia, L. Chesnel, P. Ciarlet Jr., *T*-coercivity for scalar interface problems between dielectrics and metamaterials, Math. Model. Numer. Anal. 46 (06) (2012) 1363–1387.

[17] A.-S. Bonnet-Ben Dhia, L. Chesnel, P. Ciarlet Jr., T-coercivity for the maxwell problem with sign-changing coefficients, Comm. Partial Differential Equations 39 (6) (2014) 1007–1031.

[18] H. Kettunen, L. Chesnel, H. Hakula, H. Wallén, A. Sihvola, Surface plasmon resonances on cones and wedges, in: 2014 8th International Congress on Advanced Electromagnetic Materials in Microwaves and Optics, IEEE, 2014, pp. 163–165.

[19] H.-M. Nguyen, Limiting absorption principle and well-posedness for the Helmholtz equation with sign changing coefficients, J. Math. Pure Appl. 106 (2) (2016) 342–374.

[20] A.-S. Bonnet-Ben Dhia, C. Carvalho, L. Chesnel, P. Ciarlet Jr., On the use of perfectly matched layers at corners for scattering problems with sign-changing coefficients, J. Comput. Phys. 322 (2016) 224–247.

[21] A.-S. Bonnet-Ben Dhia, L. Chesnel, M. Rihani, Maxwell's equations with hypersingularities at a conical plasmonic tip, 2020, arXiv preprint arXiv:2010.08472.

[22] C. Carvalho, Z. Moitier, Asymptotics for metamaterial cavities and their effect on scattering, 2020, arXiv preprint arXiv:2010.07583.

[23] M. Cassier, P. Joly, M. Kachanovska, Mathematical models for dispersive electromagnetic waves: An overview, Commun. Math. Anal. 74 (2017) 2792–2830.

[24] S. Nicaise, Stabilization of a Drude/vacuum model, Z. Anal. Ihre Anwe. 37 (2018) 349–375.

[25] A.-S. Bonnet-Ben Dhia, P. Ciarlet Jr., C. Zwölf, Time harmonic wave diffraction problems in materials with sign-shifting coefficients, J. Comput. Appl. Math. 234 (2010) 1912–1919, Corrigendum *J. Comput. Appl. Math.*, 234:2616, 2010.

[26] A.-S. Bonnet-Ben Dhia, L. Chesnel, X. Claeys, Radiation condition for a non-smooth interface between a dielectric and a metamaterial, Math. Models Methods Appl. Sci. 23 (09) (2013) 1629–1662.

[27] F. Frezza, F. Mangini, N. Tedeschi, Introduction to electromagnetic scattering: tutorial, J. Opt. Soc. Amer. A 35 (1) (2018).

[28] A.-S. Bonnet-Ben Dhia, C. Carvalho, P. Ciarlet Jr., Mesh requirements for the finite element approximation of problems with sign-changing coefficients, Numer. Math. 138 (4) (2018) 801–838.

[29] V. Vinoles, Regularity results for transmission problems with sign-changing coefficients: a modal approach, 2016, arXiv preprint arXiv:1611.00304.

[30] P. Johnson, R. Christy, Optical constants of the noble metals, Phys. Rev. B 6 (1972) 4370–4379.

[31] S. Lanteri, C. Scheid, J. Viquerat, Analysis of a generalized dispersive model coupled to a DGTD method with application to nanophotonics, SIAM J. Sci. Comput. 39 (3) (2017) A831–A859.

[32] K. Busch, M. König, J. Niegemann, Discontinuous Galerkin methods in nanophotonics, Laser Photon. Rev. 5 (2011) 1–37.

[33] S. Descombes, C. Durochat, S. Lanteri, L. Moya, C. Scheid, J. Viquerat, Recent advances on a DGTD method for time-domain electromagnetics, Photon. Nanostruct.: Fundam. Appl. 11 (4) (2013) 291–302.

[34] S. Lanteri, C. Scheid, Convergence of a discontinuous Galerkin scheme for the mixed time domain Maxwell's equations in dispersive media, IMA J. Numer. Anal. 33 (2) (2013) 432–459.

[35] N. Schmitt, C. Scheid, S. Lanteri, J. Viquerat, A. Moreau, A DGTD method for the numerical modeling of the interaction of light with nanometer scale metallic structures taking into account non-local dispersion effects, J. Comput. Phys. 316 (2016) 396–415.

[36] L. Chesnel, Investigation of some transmission problems with sign-changing coefficients. Application to metamaterials, (Ph.D. thesis), École Polytechnique, 2012.